

# Hydrogen Rotational and Translational Diffusion in Calcium Borohydride from Quasielastic Neutron Scattering and DFT Calculations

D. Blanchard,<sup>\*,†</sup> M. D. Riktor,<sup>‡</sup> J. B. Maronsson,<sup>†,§</sup> H. S. Jacobsen,<sup>†</sup> J. Kehres,<sup>†</sup> D. Sveinbjörnsson,<sup>†</sup> E. Gil Bardaji,<sup>||</sup> A. Léon,<sup>||</sup> F. Juranyi,<sup>⊥</sup> J. Wuttke,<sup>#</sup> B. C. Hauback,<sup>‡</sup> M. Fichtner,<sup>||</sup> and T. Vegge<sup>†</sup>

Materials Research Division, Risø National Laboratory for Sustainable Energy, Technical University of Denmark, Building 228, P.O. Box 49, DK-4000 Roskilde, Denmark, Physics Department, Institute for Energy Technology, P.O. Box 40, NO-2027 Kjeller, Norway, Center for Atomic Scale Materials Design, Technical University of Denmark, DK-2800 Lyngby, Denmark, Institute of Nanotechnology, Karlsruhe Institute of Technology (KIT), P.O. Box 3640, D-76021 Karlsruhe, Germany, Laboratory for Neutron Scattering ETH Zurich and Paul Scherrer Institut, CH- 5232 Villigen PSI, Switzerland, Forschungszentrum Jülich, JCNS at FRM II, Lichtenbergstrasse 1, 85747 Garching, Germany

Received: July 9, 2010; Revised Manuscript Received: October 8, 2010

Hydrogen dynamics in crystalline calcium borohydride can be initiated by long-range diffusion or localized motion such as rotations, librations, and vibrations. Herein, the rotational and translational diffusion were studied by quasielastic neutron scattering (QENS) by using two instruments with different time scales in combination with density functional theory (DFT) calculations. Two thermally activated reorientational motions were observed, around the 2-fold ( $C_2$ ) and 3-fold ( $C_3$ ) axes of the  $BH_4^-$  units, at temperature from 95 to 280 K. The experimental energy barriers ( $E_{aC_2} = 0.14$  eV and  $E_{aC_3} = 0.10$  eV) and mean residence times are comparable with those obtained from DFT calculations. Long-range diffusion events, with an energy barrier of  $E_{aD} = 0.12$  eV and an effective jump length of  $\sim 2.5$  Å were observed at 224 and 260 K. Three vacancy-mediated diffusion events, H jumps between two neighboring  $BH_4^-$ , and diffusion of  $BH_4^-$  and  $BH_3$  groups were calculated and finally discarded because of their very high formation energies and diffusion barriers. Three interstitial diffusion processes ( $H$ ,  $H_2$ , and  $H_2O$ ) were also calculated. The H interstitial was found to be highly unstable, whereas the  $H_2$  interstitial has a low energy of formation (0.40 eV) and diffusion barrier (0.09 eV) with a jump length (2.1 Å) that corresponds well with the experimental values.  $H_2O$  interstitial has an energy of formation of  $-0.05$  eV, and two different diffusion pathways were found. The first gives a H jump distance of 2.45 Å with a diffusion barrier of 0.68 eV, the second one, more favorable, exhibits a H jump distance of 1.08 Å with a barrier of 0.40 eV. The correlation between the QENS and DFT calculations indicates that, most probably, it is the diffusion of interstitial  $H_2$  that was observed. The origin of the interstitial  $H_2$  might come from the synthesis of the compound or a side reaction with trapped synthesis residue leading to the partial oxidation of the compound and hydrogen release.

## Introduction

Metal borohydrides are of interest as hydrogen storage materials because of their high volumetric and gravimetric capacity. However, like many of the complex hydrides, they are generally thermodynamically too stable and have slow absorption and desorption kinetics and poor reversibility.<sup>1,2</sup>

Among the borohydrides,  $Mg(BH_4)_2$  and  $Ca(BH_4)_2$  have more favorable thermodynamics than for example  $LiBH_4$  while maintaining attractive hydrogen capacities (14.9 and 11.5 mass%, respectively).<sup>2,3</sup> Furthermore, they have both been shown to be partially reversible by utilizing high pressure,<sup>4,5</sup> and  $Ca(BH_4)_2$  by utilizing additives<sup>6</sup> or destabilized routes.<sup>7</sup>

Noting the lack of knowledge about their structural transition and decomposition mechanisms, we have investigated the hydrogen dynamics in calcium borohydride by using quasielastic neutron scattering (QENS). This method is optimal to study hydrogen dynamics because of the large incoherent scattering cross section of hydrogen compared to all other scattering signals.<sup>8</sup> Although the dynamics in interstitial metal hydrides have been widely studied with neutron scattering,<sup>9–12</sup> only few published results on complex hydrides exist. As examples, the hydrogen dynamics in  $NaAlH_4$  and  $Na_3AlH_6$  were studied. It showed only limited hydrogen vacancy diffusion, not changed by the use of Ti additive.<sup>13</sup> In other work,<sup>14,15</sup> hydrogen rotational diffusion in  $NaBH_4$  was observed, but no long-range diffusion was observed.

In  $Ca(BH_4)_2$ , hydrogen is covalently bound to boron, forming tetrahedral  $BH_4^-$  complexes. The possible hydrogen dynamics are long-range translational diffusion and localized motions such as rotations of the  $BH_4^-$  complexes along specific axes, librations of the complexes, and vibrations within the complexes. Rotational dynamics are often coupled to order–disorder phase

\* Corresponding author. E-mail: dibl@risoe.dtu.dk.

<sup>†</sup> Risø National Laboratory for Sustainable Energy, Technical University of Denmark.

<sup>‡</sup> Institute for Energy Technology.

<sup>§</sup> Center for Atomic Scale Materials Design, Technical University of Denmark.

<sup>||</sup> Karlsruhe Institute of Technology.

<sup>⊥</sup> Laboratory for Neutron Scattering ETH Zurich and Paul Scherrer Institut.

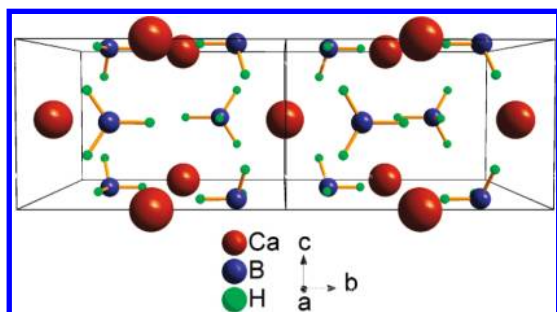
<sup>#</sup> Forschungszentrum Jülich.

**TABLE 1:**  $\beta$ -Ca(BH<sub>4</sub>)<sub>2</sub> Structural Parameters Obtained from Rietveld Refinement of PXD Pattern and DFT Calculations<sup>a</sup>

space group $P4_2/m$ (no. 84); $Z = 2$			
DFT	$a = 6.849 \text{ \AA}$	$c = 4.367 \text{ \AA}$	
PXD	7.021(6)	4.417(6)	
ref 16	(6.946(8)) <sup>b</sup>	(4.366(1))	
site	$x/a$	$y/b$	$z/c$
Ca/2c	0.5 (0.5)	0 (0)	0.5 (0.5)
B/4j	0.316 (0.302)	0.209 (0.200)	0 (0)
H1/4j	0.313 (0.295)	0.387 (0.347)	0 (0)
H2/4j	0.490 (0.468)	0.170 (0.185)	0 (0)
H3/8k	0.234 (0.226)	0.142 (0.161)	0.772 (0.800)

<sup>a</sup> In both cases, the starting values were taken from ref 16. During Rietveld refinements, the atomic positions were not refined.

<sup>b</sup> Numbers in brackets: parameters from ref 16.

**Figure 1.** Structure of  $\beta$ -Ca(BH<sub>4</sub>)<sub>2</sub>. Space group  $P4_2/m$ . Large, medium, and small spheres: Ca, B, and H atoms, respectively.

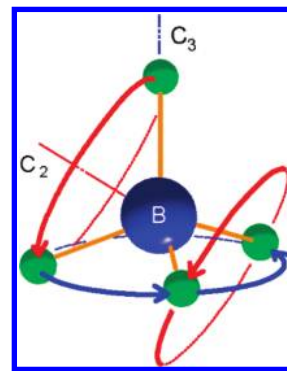
transition in coordination compounds, and the borohydrides decomposition could possibly involve long-range diffusion of H and/or of the whole BH<sub>4</sub><sup>−</sup> complexes.

At least, two different tetragonal space groups have been proposed to describe the  $\beta$ -Ca(BH<sub>4</sub>)<sub>2</sub>: Butcher et al.<sup>16</sup> chose the  $P4_2/m$  space group, whereas Filinchuk et al.<sup>17</sup> proposed  $P-4$ . The differences in the proposed structures reflect the degree of order of the BH<sub>4</sub><sup>−</sup> units. The possibility to refine the  $\beta$ -structure in different tetragonal space groups with different BH<sub>4</sub><sup>−</sup> orientations suggests that the polymorph is stabilized by static or dynamic disorder of the borohydride units like for the high-temperature polymorphic transformation of LiBH<sub>4</sub>.<sup>18–20</sup> For the Rietveld refinement as well as for the DFT calculations, the  $P4_2/m$  space group and the crystallographic data from ref 16 were used (Table 1). Ca(BH<sub>4</sub>)<sub>2</sub> forms ionic crystals consisting of Ca<sup>2+</sup> and BH<sub>4</sub><sup>−</sup> ions. The Ca<sup>2+</sup> ions are coordinated by six BH<sub>4</sub><sup>−</sup> tetrahedra in a bidendate configuration. The B–H interatomic distances are in the range of 1.1 Å, and the Ca–Ca distances are about 4.35 Å (Figure 1). There are two formula units per unit cell. The Ca atoms occupy the (2c) Wyckoff positions, the B atoms occupy the (4j) positions, and the H atoms are distributed over the (4j) and (8k) sites. The BH<sub>4</sub><sup>−</sup> tetrahedra possess three 2-fold rotational symmetries (C<sub>2</sub>) and four 3-fold rotational symmetries (C<sub>3</sub>) leading to three 180° and four 120° rotations (Figure 2).

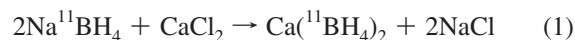
Herein, the aim was to investigate the rotational and long-range translational diffusion of H-rich species in  $\beta$ -Ca(BH<sub>4</sub>)<sub>2</sub>. Therefore, QENS combined with density functional theory (DFT) calculations have been applied.

## Material and Experimental Methods

Natural B contains 20% of <sup>10</sup>B which has a high absorption cross section of 3837 barns. Therefore, to reduce neutron

**Figure 2.** 2-fold C<sub>2</sub>-axis and 3-fold C<sub>3</sub>-axis of the BH<sub>4</sub><sup>−</sup> units. Large and small spheres: B and H atoms, respectively.

absorption, Ca(BH<sub>4</sub>)<sub>2</sub> was synthesized via the metathesis reaction of eq 1 by using a <sup>11</sup>B-enriched precursor (5.5 × 10<sup>−3</sup> barns).



A total of 2.40 g (0.063 mol) of Na<sup>11</sup>BH<sub>4</sub> (purchased from Katchem Ltd., purity 99.8%) was first ball-milled for 4 h in a Fritsch P6 planetary mill at 600 rpm, with a ball-to-powder ratio of 25:1, and then added to 3.52 g (0.032 mol) of CaCl<sub>2</sub> (purchased from Alfa Aesar, purity 96%) in 100 mL of THF. The mixture was heated under reflux at 80 °C for 24 h. After cooling to room temperature, the suspension was filtered off, and the filtrate was evaporated under vacuum to remove the solvent. The resulting Ca(<sup>11</sup>BH<sub>4</sub>)<sub>2</sub>·*n* THF adduct was then dried at elevated temperature under vacuum (at 80 °C for 2 h, at 100 °C for 2 h, at 130 °C for 1 h, at 160 °C for 1 h, and at 200 °C for 16 h). The isolated yield (with respect to CaCl<sub>2</sub>) was 2.0 g (90%).

Calcium borohydride crystallizes in different structure modifications depending on the synthesis conditions, and a mixture of the three structures,  $\alpha$ -Ca(BH<sub>4</sub>)<sub>2</sub>,  $\beta$ -Ca(BH<sub>4</sub>)<sub>2</sub>,<sup>16,21</sup> and  $\gamma$ -Ca(BH<sub>4</sub>)<sub>2</sub> may be formed. The drying procedure used during the synthesis aimed to obtain  $\beta$ -Ca(BH<sub>4</sub>)<sub>2</sub> as a single phase.

A powder X-ray diffraction (PXD) was recorded with a BRUKER D8 diffractometer (40 kV, 40 mA, Cu radiation K<sub>α</sub> = 1.542 Å, Figure 3). Quantitative phase analysis based on Rietveld refinements performed by using Rietica software<sup>22</sup> gave a molar composition of 85%  $\beta$ -Ca(BH<sub>4</sub>)<sub>2</sub>, 6%  $\alpha$ -Ca(BH<sub>4</sub>)<sub>2</sub>, 4% CaH<sub>2</sub>, and 5% NaCl, and thus, ~93% of the hydrogen in the sample belongs to  $\beta$ -Ca(BH<sub>4</sub>)<sub>2</sub>. Only the cell parameters were refined. For CaBH<sub>4</sub> (see Table 1), they are slightly larger than those in ref 16, probably because of the quality of the diffraction pattern; but they are still in reasonable agreement.

Mass spectrometry measurements (MS), obtained by using an OmniStar (GSD 320) mass spectrometer, were performed on the gas released by the sample when heated under dynamical vacuum from room temperature up to 723 K (heating ramp of 1 K min<sup>−1</sup>, Figure 4). The analysis of the measurement shows that H<sub>2</sub> accounts for ~98.7% of the released gas, and THF accounts for ~1.2%; the amount of H<sub>2</sub>O, B<sub>2</sub>H<sub>6</sub>, and other gases such as O<sub>2</sub> are negligible (<1%). Thus, the amount of THF left in the sample after its synthesis is very low, and the sample appears to be water free.

QENS experiments were performed with two complementary instruments, SPHERES and MARS, in order to cover a wide energy range with two different energy resolutions. SPHERES<sup>23</sup> is a high-resolution neutron backscattering spectrometer located

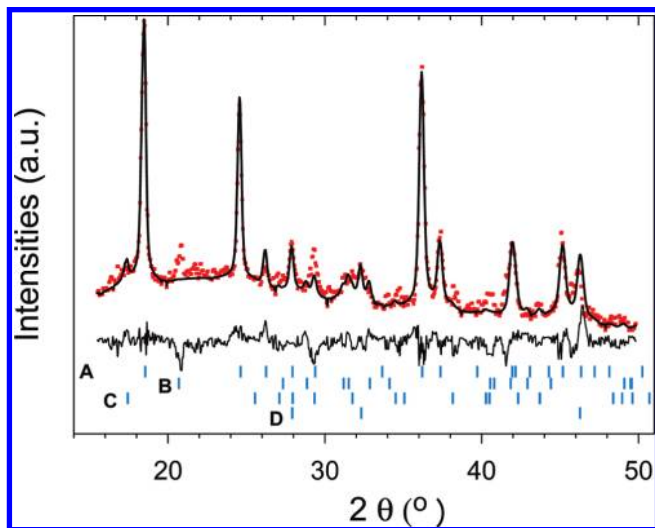


**Figure 3.** PXD pattern of the as-prepared  $\beta\text{-Ca}(\text{BH}_4)_2$ . The dots are the experimental points, the line is the refined pattern based on the Rietveld method, and the bottom line is the difference between the experimental and the refined pattern. The ticks are the position of the Bragg peaks for A:  $\beta\text{-Ca}(\text{BH}_4)_2$ , B:  $\text{CaH}_2$ , C:  $\alpha\text{-Ca}(\text{BH}_4)_2$ , and D:  $\text{NaCl}$ .

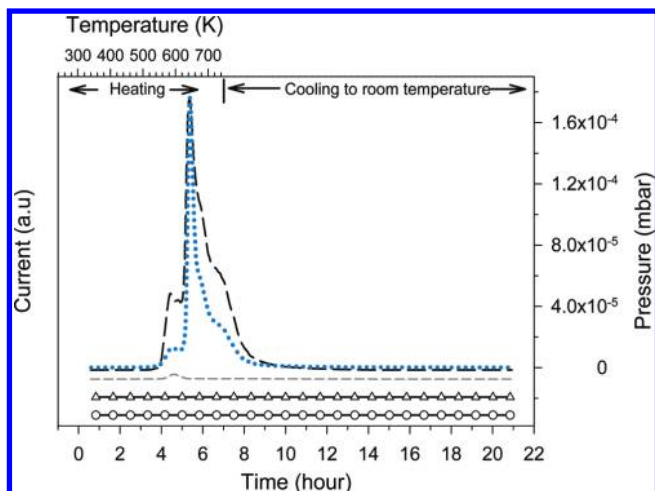


**Figure 4.** Mass spectrometry measurements. The sample was heated under dynamical vacuum from room temperature up to 723 K at a heating ramp of  $1\text{ K}\cdot\text{min}^{-1}$ . Dotted line, pressure evolution; long dashed line,  $\text{H}_2$  signal; short dashed line, THF signal; circles,  $\text{B}_2\text{H}_6$  signal; triangles,  $\text{H}_2\text{O}$  signal.

at FRM II (Forschungs-Neutronenquelle Heinz Maier-Leibnitz), Garching, Germany. MARS<sup>24</sup> is an inverted geometry time-of-flight spectrometer located at the Swiss Spallation Neutron Source (SINQ), Paul Scherrer Institute, Villigen, Switzerland.

The experiments at SPHERES were performed with  $\sim 0.1$  g of  $\text{Ca}(\text{BH}_4)_2$ , which was loaded in an Al wire sealed flat  $30 \times 40 \times 0.5$  mm<sup>3</sup> Al container oriented at  $135^\circ$  with respect to the direct beam. Si(111) monochromator and analyzer crystals were used in a backscattering geometry, giving a final neutron wavelength of 6.271 Å and an energy resolution of 0.65  $\mu\text{eV}$  with an energy-transfer range selected within  $\pm 15.8$   $\mu\text{eV}$ . The spectra were recorded by nine detectors corresponding to a scattering vector ranging from 0.59 to 1.66 Å<sup>−1</sup>. The data reduction was carried out with SLAW, a neutron histogram to scattering law converter.<sup>25</sup>

The experiments at MARS were performed with  $\sim 0.4$  g of  $\text{Ca}(\text{BH}_4)_2$ , from the same batch, which was loaded in a double-wall Al container with a height of 60 mm and diameters of 9 mm and 10 mm. The spectra were recorded by five detectors

on both side of the instrument corresponding to a scattering vector ranging from 0.49 to 1.86 Å<sup>−1</sup>. Mica(006) analyzers were used in a near-backscattering geometry, giving a final neutron wavelength of 6.65 Å and an energy resolution of 13  $\mu\text{eV}$ . The energy-transfer window was chosen differently depending on the width of the quasielastic signal, the largest being from  $-0.04$  to 0.43 meV. The data reduction was carried out with the data analysis and visualization environment DAVE.<sup>25</sup>

### DFT Calculations

Theoretical calculations were used to identify the possible dynamic events by calculating their energy barriers and prefactors. The calculations were performed by using the atomic simulation environment (ASE) package,<sup>27</sup> and the DACAPO plane-wave basis-set implementation<sup>28</sup> was used to solve the electronic structure problem within the DFT formalism.<sup>29</sup> The ion cores were described by ultrasoft pseudopotentials,<sup>30</sup> and the exchange and correlation effects were described by the PW91 functional.<sup>31</sup> The Kohn–Sham wave functions were expanded in a plane-wave basis set with a cutoff energy of 350 and 600 eV for the density grid cutoff. The wave functions were sampled on a  $(2 \times 2 \times 2)$  k-point mesh. The unit cell containing 2  $\text{Ca}(\text{BH}_4)_2$  units was the  $\beta$ -phase structure.<sup>16</sup> To eliminate any spurious periodic interactions, the calculations were carried out on a 176 atoms supercell, which consisted of the unit cell repeated once in each spatial direction. Iterative relaxation using the limited memory Broyden–Fletcher–Goldfarb–Shanno algorithm<sup>32</sup> was employed to obtain the zero-temperature structure and unit-cell parameters. A force convergence criterion of 0.001 eV/Å was used for the structure minimization.

The nudged elastic band (NEB) method,<sup>33</sup> along with the FIRE minimization algorithm,<sup>34</sup> was used to locate first-order saddle-point configurations, connecting two local minima, that could be used within harmonic transition state theory (hTST)<sup>35</sup> to determine the thermally activated reaction rates ( $r(T)$ ) by using the barrier height ( $E_a$ ) and the vibrational frequencies at the initial state ( $\nu^{\text{IS}}$ ) and saddle point ( $\nu^{\text{TS}}$ ).

$$r(T) = \frac{\prod_{i=1}^{3N} \nu_i^{\text{IS}}}{\prod_{i=1}^{3N-1} \nu_i^{\text{TS}}} e^{-\frac{E_a}{k_B T}} \quad (2)$$

The vibrational frequencies were acquired by using a finite difference approximation of the Hessian matrix (back and forward displacements of 0.01 Å). The term outside the exponential in eq 2, often referred to as the prefactor, compares the vibrational frequencies at the initial state and saddle point. The characteristic times are the reciprocal values of these prefactors.

A force convergence criterion of 0.01 eV/Å was used for the NEB calculations that lead to vibrational frequencies calculations and 0.05 eV/Å for the NEB calculations that only considered the barriers.

The initial paths used when locating the rotational pathways were simple rigid rotations of all the hydrogen atoms in a single  $\text{BH}_4^-$  unit.

To calculate diffusion, vacancies were created by removing the atom(s) in question and rereleasing the atomic coordinates. Similarly, interstitials were created by inserting the atom(s) in question and rereleasing the atomic coordinates. Neighboring, relaxed, defect structures were then used as end points in linearly interpolated NEB calculations.



**TABLE 2: Summary of the Experimental (QENS, Rotational and Translational Diffusion) and Computational (DFT, Rotational Diffusion) Results for  $\beta$ -Ca(BH<sub>4</sub>)<sub>2</sub>**

$\tau_0^a$ (ps)		$E_a^a$ (eV)	
MARS and SPHERES			
<b>C<sub>3</sub></b>	<b>C<sub>2</sub></b>	<b>C<sub>3</sub></b>	<b>C<sub>2</sub></b>
$5.0 \times 10^{-2}$	$5.6 \times 10^{-2}$	0.10	0.14
long-range diffusion			
4			0.12
DFT			
<b>C<sub>3</sub></b>	<b>C<sub>2</sub></b>	<b>C<sub>3</sub></b>	<b>C<sub>2</sub></b>
$1.87 \times 10^{-2}$	$3.97 \times 10^{-2}$	0.11	0.15

<sup>a</sup>  $\tau_0$  and  $E_a$  experimental values obtained from the Arrhenius fits ( $\tau = \tau_0 \exp(E_a/(k_b T))$ ) of the experimental mean resident times.

**TABLE 3: Summary of the Computational (DFT, Translational Diffusion) Results for  $\beta$ -Ca(BH<sub>4</sub>)<sub>2</sub>**

defect type	formation energy (eV) <sup>a</sup>	$\tau_0$ (ps)	$E_{ad}$ (eV)	diffusion length (Å)
H vacancy	2.09	$8.0 \times 10^{-1}$	0.46	2.1
BH <sub>3</sub> vacancy	1.56	$6.1 \times 10^{-2}$	1.92	3.3
BH <sub>4</sub> vacancy	2.83	N/A <sup>b</sup>	0.63	3.8
H interstitial	2.34 <sup>c</sup>	N/A	N/A	N/A
H <sub>2</sub> interstitial	0.40	$5.68 \times 10^{-2}$	0.09	2.1
H <sub>2</sub> O inter. flip	-0.05	N/A	0.40	1.08
H <sub>2</sub> O interstitial	-0.05	N/A	0.68	2.45

<sup>a</sup> The formation energies were calculated for neutral species. <sup>b</sup> N/A: not calculated. <sup>c</sup> The H interstitial is not stable and relaxes to a H<sub>2</sub> interstitial coupled to a H vacancy.

## Results

**QENS Spectra.** Inelastic temperature scans were performed on both instruments. For each temperature, the spectra collected on each detector were summed to get one spectra. The elastic intensities were obtained by adding up the counts with an energy transfer of  $|\delta E| \leq 8 \mu\text{eV}$  and  $|\delta E| \leq 0.32 \mu\text{eV}$  for MARS and SPHERES, respectively. The inelastic intensities were deduced by summing up the counts out of the elastic regions. Figure 5 displays the evolution with temperature of the normalized elastic ( $I_{N-el}$ ) and inelastic ( $I_{N-inel}$ ) scattering measured at MARS and SPHERES. The sample was heated from 70 to 565 K at MARS. At 70 K, no inelastic broadening was detected because the hydrogen is frozen-in on the time scale accessible with the instrument. On heating between 70 and 120 K,  $I_{N-el}$  ( $|\delta E| \leq 8 \mu\text{eV}$ ) slowly decreased, whereas  $I_{N-inel}$  ( $|\delta E| > 8 \mu\text{eV}$ ) slowly increased; then, the same evolution is continued only faster. The maximum  $I_{N-inel}$  is at 200 K followed by a decrease and then no more changes. At this temperature and above, the hydrogen motion is too fast, and the large inelastic broadening gives a flat background. When cooling from 565 to 200 K,  $I_{N-el}$  is identical to that observed during heating, whereas  $I_{N-inel}$  is found to be lower. At  $T < 200$  K,  $I_{N-el}$  is also found to be lower than on heating, indicating a loss of  $\sim 18\%$  (weakly) bound hydrogen, that has been desorbed during heating. The MS measurement revealed a slight release of hydrogen between 520 and 565 K, corresponding to  $\sim 4\%$  of the total hydrogen released during the measurement up to 723 K (see Figure 4). Similar observations have been made in several other published studies.<sup>36–38</sup> In ref 38, the sample, heated up to 603 K, was quenched and examined with high-resolution synchrotron radiation powder diffraction. Along with  $\beta$ -Ca(BH<sub>4</sub>)<sub>2</sub>, Bragg peaks from an unknown phase were observed, which have recently been identified and structurally resolved as an oxide of the borohydride.<sup>39</sup> PXD measurements made on the sample used

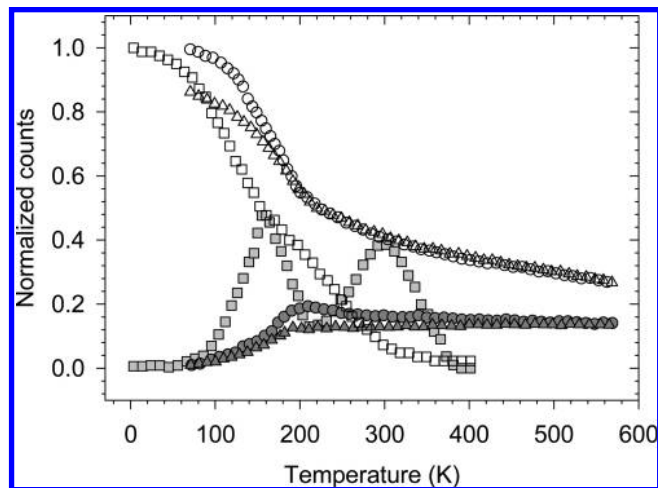


**Figure 5.** Normalized elastic and inelastic intensities ( $I_{N-el}$  and  $I_{N-inel}$ ) during temperature scans. Open and filled  $\circ$ :  $I_{N-el}$  and  $I_{N-inel}$ , respectively, with MARS on heating from 70 to 570 K. Open and filled  $\triangle$ :  $I_{N-el}$  and  $I_{N-inel}$ , respectively, with MARS on cooling from 570 to 70 K. Open and filled  $\square$ :  $I_{N-el}$  and  $I_{N-inel}$ , respectively, with SPHERES on heating from 3 to 400 K.

for the temperature scans with MARS (not shown herein) also revealed the presence of this oxide phase. Thus, the hydrogen release observed during the MS measurement and temperature scan might come from a reaction of the hydride with oxygen or water. The oxygen level remains in the background level during the MS; therefore, one can exclude the existence of a leak in the experimental setup, and the only source of oxygen or water comes from the sample itself, without excluding a possible reaction with residual THF.

At SPHERES, the temperature scan (Figure 5) was performed only during heating. It showed almost the same features as those for the MARS measurements, but changes occurred at lower temperatures. The inelastic intensity ( $|\delta E| \leq 0.32 \mu\text{eV}$ ) starts to increase at around 80 K, with the maximum at 160 K, and decreases significantly afterward. However, at 220 K,  $I_{N-inel}$  ( $|\delta E| > 0.32 \mu\text{eV}$ ) increases again with a maximum at 320 K followed by a decrease and then flatten out at 390 K. At this temperature, the hydrogen motion gives rise to a broadening too large for the instrument energy window. The two bumps in the inelastic signal were attributed to two different types of hydrogen dynamics, as it will be discussed below.

The temperatures to perform the measurements were selected from these scans (see Table 4). The QENS spectra were analyzed by using the curve fitting utility (PAN) included in the DAVE package. They consist of one elastic and some inelastic components. The elastic component comes from the scattering process with no change in the neutron energy, whereas the inelastic component reflects the energy transfer, gain, and loss, due to the hydrogen motions. The measured total incoherent scattering function,  $S_{inc}^{tot}(Q\omega)$ , is given by (see ref 8 for more details):

$$S_{inc}^{tot}(Q\omega) = R(Q\omega) \otimes (A_0(Q)\delta(\omega) + \sum_i A_i(Q)L(\Gamma_i, \omega)) + B(Q) \quad (3)$$

where  $R(Q, \omega)$  is the instrumental resolution,  $\delta(\omega)$  is the Dirac delta function describing the elastic scattering.  $L(\Gamma_i, \omega)$  are Lorentzian functions which model the inelastic signal with  $\Gamma_i$  = half width at half maximum (HWHM). The  $B$  term represents

**TABLE 4: Summary of the Experimental (QENS) Results for  $\beta$ -Ca(BH<sub>4</sub>)<sub>2</sub>**

temp. (K)	$\tau$ (ps)	
	C <sub>3</sub>	C <sub>2</sub>
MARS		
100	204	-
130	145	-
160	40	-
190	17	245
220	8	82
280	3	32
SPHERES		
95	6582	-
116	429	-
143	141	7520
163	58	1755
204	-	131
long-range diffusion		
224	2302	
260	977	

the inelastic background in the quasielastic region. It can originate from processes that are much faster than those observable within the time scale of the instruments used. The term  $A_0(Q)$  is the elastic incoherent structure factor (EISF).<sup>8</sup> Its dependence on  $Q$ , the wave vector transfer, is important. It basically determines the static properties of the number of sites accessible to the hydrogen atoms, the locations of these sites, and the normalized probability to be at a given sites. It is a measurable quantity, evaluated from the ratio:

$$A_0(Q) = \frac{I_{el}(Q)}{I_{el}(Q) + I_{inel}(Q)} \quad (4)$$

where  $I_{el}(Q)$  and  $I_{inel}(Q)$  are the integrated intensities of the elastic and inelastic signal, respectively.

Herein and following eq 3, the QENS spectra were analyzed with the resolution-limited elastic peak, the delta function folded with the instrumental resolutions, and one or two Lorentzian, depending on the temperature. The instrumental resolutions were obtained from measurements at 3 K (SPHERES) and 70 K (MARS). At these temperatures, no dynamical motions were observed on the time scale of the two instruments. The centers of the delta function and of the Lorentzian were constrained to be the same. For the measurements performed at MARS, because the energy window of the resolution function was smaller than those used for the measurements at higher temperatures, a flat fixed background was used. For the measurements performed at SPHERES, a flat background was used to model the too broad Lorentzian at high temperatures. Figures 6 and 7 present typical examples of the spectra together with their fits with one or two Lorentzian. For the whole temperature range measured at MARS, and at least up to 220 K at SPHERES, the widths of the Lorentzian functions were found to be  $Q$ -independent over the measured  $Q$  range. This indicates that the observed inelastic broadenings originate from localized hydrogen motion.<sup>8</sup> Figure 8 displays the values of the average HWHMs, over all the detectors, versus temperature. At SPHERES, for two temperatures above 220 K (224 and 260 K), the HWHMs were found to be  $Q$ -dependent (Figure 11), a signature for nonlocalized motion and possibly long-range diffusion. Unfortunately, at higher temperature, the fits of the QENS spectra are no longer reliable because of the low signal

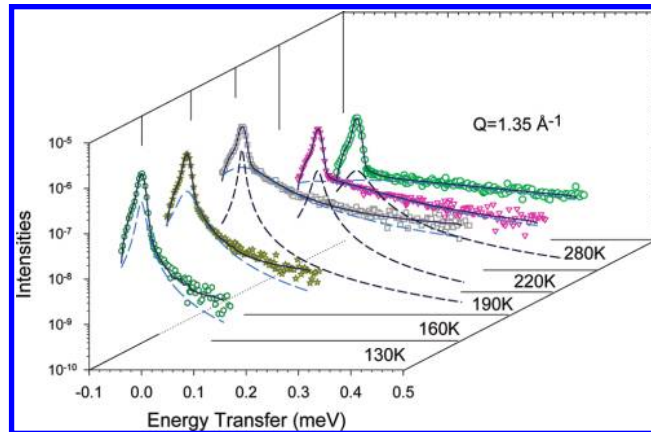


**Figure 6.** QENS of  $\beta$ -Ca(BH<sub>4</sub>)<sub>2</sub> measured with MARS at different temperatures for  $Q = 1.35 \text{ \AA}^{-1}$ . The dots are the experimental data. The solid lines display the fits of the data, each consisting of a resolution-broadened delta function, a flat background, and one or two Lorentzian (dashed line).

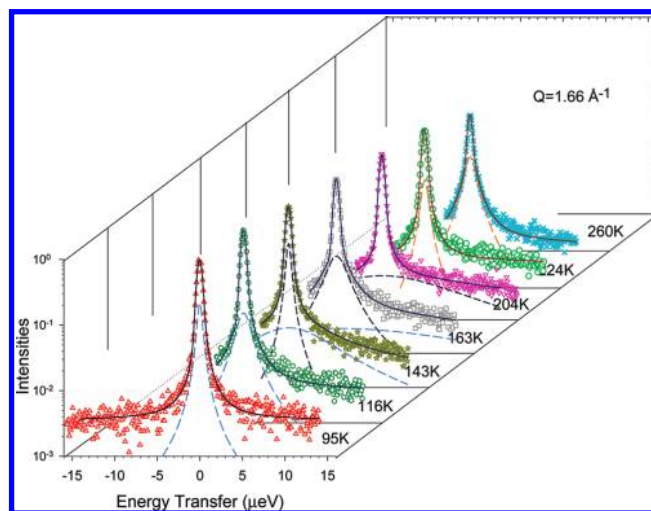


**Figure 7.** QENS of  $\beta$ -Ca(BH<sub>4</sub>)<sub>2</sub> measured with SPHERES at different temperatures for  $Q = 1.66 \text{ \AA}^{-1}$ . The dots are the experimental data. The solid lines display the fits of the data, each consisting of a resolution-broadened delta function, one or two Lorentzian (dashed line), and a flat background for the three last temperatures (not shown on the plots).

intensity combined with the too broad inelastic component at high  $Q$  values.

The first obvious localized motions are the rotations around the 2-fold and 3-fold axis (Figure 2). For BH<sub>4</sub><sup>-</sup> rotations around the C<sub>2</sub>-axis, the tetrahedral ions have two equal equilibrium orientations, and the EISF is:<sup>8</sup>

$$A_0(Q) = \frac{1}{2} \left( 1 + j_0 \left( 2 \frac{\sqrt{2}}{\sqrt{3}} Qd \right) \right) \quad (5)$$

where  $j_0(x) = \sin(x)/x$  is the zeroth order Bessel function and  $d$  is the bond length between B and H. This rotation gives rise to one Lorentzian with a  $Q$ -independent HWHM of

$$\Gamma_{C2} = 2\hbar\tau_2^{-1} \quad (6)$$

$\tau_2$  represents the average time that a hydrogen atom stays at a site before jumping to a new site because of reorientation around the 2-fold axis.

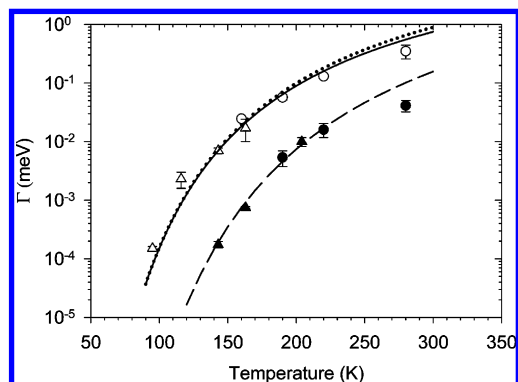


**Figure 8.** Experimental and theoretical HWHMs. The dots are the averaged, over all the detectors, experimental values. Triangles, SPHERES data; circles, MARS data. The theoretical values are calculated from eqs 9–11, with values of the characteristic times, energy barriers, and prefactors obtained from DFT. Dotted line, HWHMs calculated from eq 9; solid line, HWHMs calculated from eq 10; dashed line, HWHMs calculated from eq 11.

For  $\text{BH}_4^-$  rotations around the  $\text{C}_3$ -axis, the tetrahedral ions have three equal equilibrium orientations, and one hydrogen atom remains immobile. The expression for the EISF is identical to the rotation around the  $\text{C}_2$ -axis (eq 5).<sup>8</sup> It gives rise to one Lorentzian with a  $Q$ -independent HWHM of

$$\Gamma_{\text{C}_3} = \frac{3}{2} \hbar \tau_3^{-1} \quad (7)$$

$\tau_3$  represents the average time that a hydrogen atom stays at a site before jumping to a new site because of reorientation around the 3-fold axis.

In the case of combination of rotations around several  $\text{C}_2$  and  $\text{C}_3$ -axis, with two different jump rates, the EISF is given by:<sup>15</sup>

$$A_0(Q) = \frac{1}{4} \left( 1 + j_0 \left( Q \frac{2\sqrt{2}}{\sqrt{3}} d \right) \right) \left( 1 + j_0 \left( Q \frac{2\sqrt{2}}{\sqrt{3}} d \right) \right) \quad (8)$$

The combination of these two rotations gives rise to three Lorentzian with the following  $Q$ -independent HWHMs:

$$\Gamma_1 = \hbar(2\tau_2^{-1} + \frac{3}{2}\tau_3^{-1}) \quad (9)$$

$$\Gamma_2 = \frac{3}{2} \hbar \tau_3^{-1} \quad (10)$$

$$\Gamma_3 = 2 \hbar \tau_2^{-1} \quad (11)$$

with  $\tau_2$  and  $\tau_3$  defined above.

The experimental EISFs, extracted from the fitted QENS spectra (eq 4), and those calculated with the models described above (eqs 5 and 8) provide strong evidence about the nature of the localized motions. Figure 9 displays the EISFs. The model for one rotation (eq 5) follows the experimental data when one inelastic component was detected in the QENS spectra (95 and 204 K with SPHERES, 130 and 160 K with MARS). The model combining the two rotations ( $\text{C}_2$ – $\text{C}_3$ , eq 8) reproduces the experimental EISFs when two Lorentzian were needed to fit the QENS spectra (116–163 K with SPHERES, 190 K and

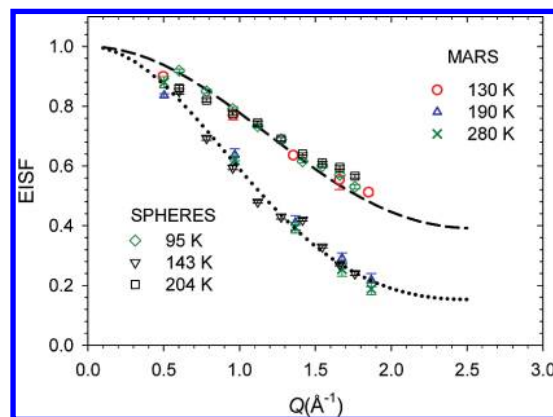


**Figure 9.** Measured and modeled EISFs. Dashed line,  $\text{C}_3$  rotational diffusion model according to eq 5; dotted line, combination of  $\text{C}_2$ – $\text{C}_3$  rotational diffusion model according to eq 8. Not all the temperatures have been plotted in order to keep the figure clear.

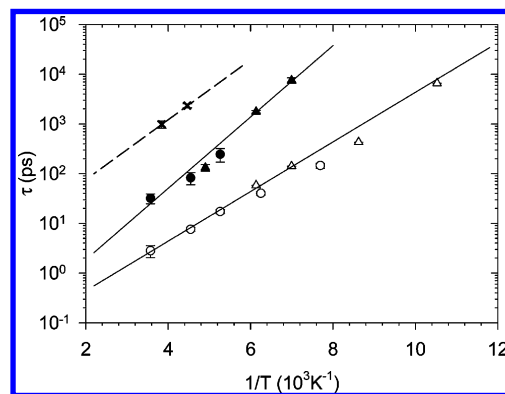


**Figure 10.** Thermally activated Arrhenius behavior of the rotational and translational diffusion of H in  $\beta\text{-Ca}(\text{BH}_4)_2$ . The triangles are the SPHERES experimental mean residence time ( $\tau$ ) and the circles the MARS experimental values. Filled symbols: rotation around the  $\text{C}_2$  axis, open symbols rotation around the  $\text{C}_3$  axis. The cross symbols are the mean resident time between two diffusional jumps (data from SPHERES).  $\tau$ , inversely proportional to the inelastic broadening, is fitted as  $\tau_0 \exp((E_a)/(k_B T))$  with  $\tau_{0\text{C}_2} = 5.6 \times 10^{-2}$  ps,  $E_{a\text{C}_2} = 0.14$  eV and  $\tau_{0\text{C}_3} = 5.0 \times 10^{-2}$  ps,  $E_{a\text{C}_3} = 0.10$  eV. The broken line is the fit for the diffusional jumps ( $E_{aD} = 0.12$  eV, prefactor  $\tau_{0D} = 4.7$  ps).

above with MARS). For both equations, the best fit was obtained for  $d = 1.11$  Å, a value in agreement with the B–H distance obtained from neutron-diffraction data.<sup>15</sup> The characteristic times of the localized hydrogen motion, now attributed to reorientational rotations, were calculated from the average HWHMs at a given temperature. Equations 9–11 were used. In the case of the low-temperature spectra, fitted with one Lorentzian,  $\tau_2$  was considered as infinite. The results are presented in Table 4. The observed inelastic broadening follows an Arrhenius behavior, and the corresponding characteristic times can be expressed as

$$\tau = \tau_0 \exp\left(\frac{E_a}{k_B T}\right) \quad (12)$$

where the prefactor  $\tau_0$  is a constant,  $E_a$  is the energy barrier for the motion,  $k_B$  is the Boltzmann constant, and  $T$  is the temperature. Figure 10 displays the experimental characteristic times of the two thermally activated rotations together with the Arrhenius fits. The following values are obtained for the energy barriers: 0.14 and 0.10 eV for the  $\text{C}_2$  and the  $\text{C}_3$  rotations, respectively (see Table 4).



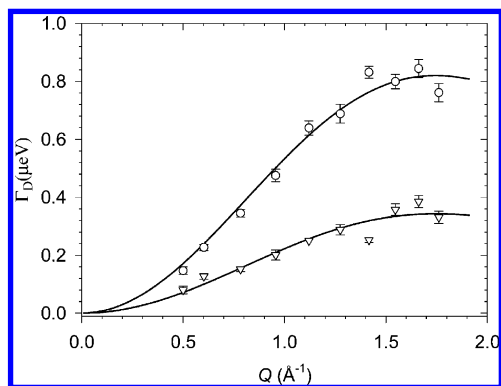


**Figure 11.** HWHM of the Lorentzian QENS component for  $\beta\text{-Ca}(\text{BH}_4)_2$ , as a function of  $Q$  measured with SPHERES, at 224 K ( $\nabla$ ) and 260 K (o). The full curves show the fits of the Chudley–Elliott model (eq 13) to the data.

For a nonlocalized motion, for example, long-range translational diffusion, the inelastic line broadening is  $Q$ -dependent.<sup>8</sup> Because hydrogen diffusion in complex hydrides can be vacancy-mediated, it must be taken into account that only the motion of the vacancy can be considered as random walk, whereas the involved atomic motions are correlated. Thus, the so-called encounter model should be used to describe the correlated jumps.<sup>40</sup> Nevertheless, in a zero-order approximation, that is, one atomic jump per stochastic vacancy diffusion step, the Chudley–Elliott model<sup>41</sup> can be used. The only effect is a rescaling of  $\tau_D$ , the mean time between two jumps.<sup>40,42,43</sup> In the Chudley–Elliott model, the  $Q$ -dependence of the HWHM ( $\Gamma_D$ ) is given by<sup>8</sup>

$$\Gamma_D(Q) = \frac{\hbar}{\tau_D} \left( 1 - \frac{\sin(QL)}{QL} \right) \quad (13)$$

where  $L$  is the effective jump length.  $\tau_D$  and  $L$  were extracted from the fits of the Chudley–Elliott model to the data obtained with SPHERES at 224 and 260 K (see Figure 11 and Table 4). The effective jump length was found to be about 2.5 Å (it corresponds to the shortest H–H distance between two neighboring  $\text{BH}_4^-$  groups). An Arrhenius fit to the QENS data for the two available temperatures yields an energy barrier of  $E_{\text{ad}} = 0.12$  eV and a prefactor of  $\tau_{0D} = 4.7$  ps (see Figure 10 and Table 2).

**DFT Calculations.** The calculated structural parameters for the relaxed  $\beta\text{-Ca}(\text{BH}_4)_2$  are displayed in Table 1. The Wyckoff positions and cell parameters are in good agreement with those from ref 16.

The results from the QENS experiments indicated localized dynamic events such as rotations of borohydride units as well as possible high-temperature diffusion. When using the Schönflies notation,<sup>44</sup> there are four different types of permutations possible for a single tetrahedral borohydride group. S4 axes and mirror planes can be quickly discarded because they are not rotations but rearrangements of hydrogen atoms which are much higher in energy because of the required formation of a planar  $\text{BH}_4$  configuration during the rearrangement. Then, only various  $C_2$  and  $C_3$  axes remain. Figure 12 presents a 2D rigid rotation potential energy surface (PES) calculated by using a  $C_2$ -axis and a  $C_3$ -axis of a single  $\text{BH}_4^-$  as the degrees of freedom. The starting point for the calculation is the relaxed structure, and thus, the origin of the axis represents an energy minimum. As expected from their symmetry, energy minima for the rotations around the  $C_2$ -axis occur at  $\pi$  and around the  $C_3$ -axis at  $(2\pi)/3$

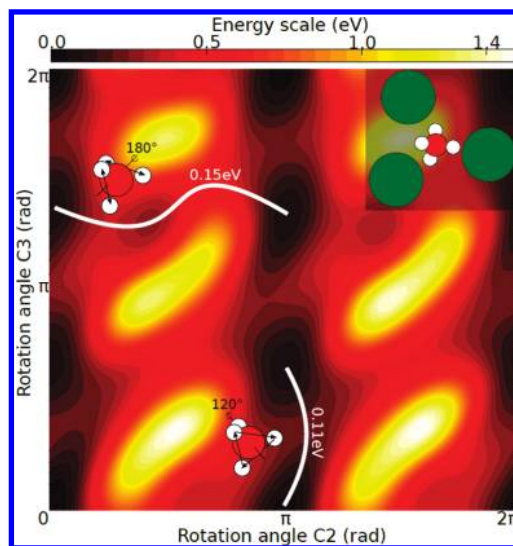


**Figure 12.** PES for  $\text{BH}_4^-$  rigid rotations along the  $C_2$ -axis and  $C_3$ -axis. The marked paths represent those chosen to do the NEB calculations. Their respective NEB barrier heights are written next to each one. The inset shows the immediate environment of a  $\text{BH}_4^-$  unit. Large, medium, and small spheres: Ca, B, and H atoms, respectively.

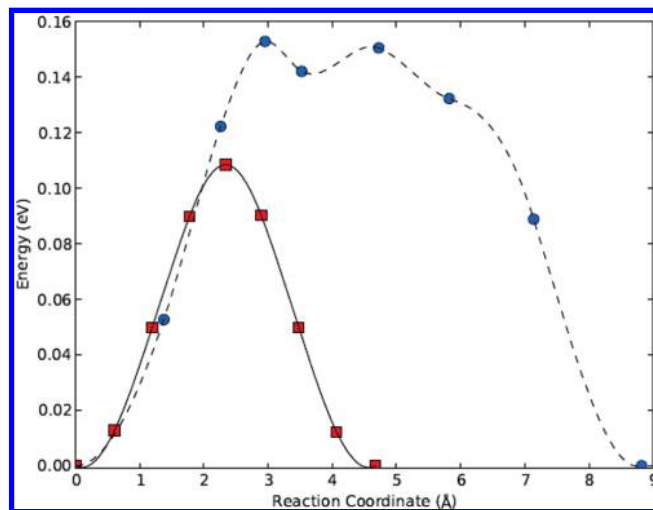


**Figure 13.** Calculated minimum energy path for the  $C_2$  (blue circles) and  $C_3$  (red squares) rotations. Each point is an NEB image; the lines are interpolations between them obtained by using also the forces. The reaction coordinate is the additive motion of atoms in the supercell.

and  $(4\pi)/3$ . It shows that a slightly distorted  $C_3$  rotation yields the lowest barrier and that a wobbly  $C_2$ -like rotation has a somewhat higher barrier (a difference of approximately 80%). The barrier heights calculated from the rigid rotation being higher than the barriers suggested by the experiments, NEB calculations were carried out with all the atoms in the supercell free to move. These calculations yielded barriers and characteristic times in good quantitative agreement with those of the experiments (see Table 2 and Figure 13). The calculated characteristic time for  $C_2$  is about twice that of  $C_3$ . Looking at Figure 12, it can be seen that the environment of the saddle points for each rotation are quite different, and the vibrational calculations also revealed modes that involve motion of the cations, different by roughly a factor of 2. These findings are in reasonable agreement with experiments, where the prefactor for  $C_2$  is found to be 10% larger than the one for  $C_3$ .

The theoretically expected temperature dependences of the HWHMs of the QENS spectra are plotted in Figure 8 together with the experimental values. The calculated lines were obtained

by using eqs 9–11, with the characteristic times obtained by using the Arrhenius law (eq 12) and the energy barriers and prefactors from the DFT calculations. According to the experimental results, it should be noted that, although the combination of the two rotations ( $C_2$ – $C_3$ ) should give three Lorentzian, two have comparable HWHMs ( $\Gamma_1 \approx \Gamma_2$ ) and can hardly be separated experimentally.

With two rotations unambiguously identified, only one dynamic event involving nonlocalized motion remained unexplained. Because further rotation could be ruled out, the diffusion process should be analyzed. Three vacancy-mediated diffusion events, H jumps between two neighboring  $BH_4^-$ , and diffusion of  $BH_4^-$  and  $BH_3$  groups, were calculated. All were found to have high formation energies of the corresponding neutral vacancies and high diffusion energy barriers (see Table 3). Subsequently, interstitial-mediated diffusion of H,  $H_2$ , and  $H_2O$  were considered. The H interstitial is found to be unstable and formed a  $H_2$  interstitial coupled to a H vacancy on a  $BH_4^-$ , with a very high formation energy (see Table 3).  $H_2O$  and  $H_2$  interstitials were found to have low formation energies, that is,  $-0.05$  and  $0.4$  eV, respectively. Two pathways were identified for  $H_2O$  diffusion, one involving a flip of the molecule and one giving a longer jump distance with a higher energy barrier; nevertheless, both pathways exhibit values slightly different from the experimental ones. Only interstitial  $H_2$  diffusion gave a barrier and jump length which corresponds well to the experimentally observed value (Tables 2 and 3). The agreement between the calculated characteristic time for  $H_2$  diffusion and the one obtained experimentally is not absolute; however it should be noted that the later was extracted from an Arrhenius fit with only two points. It is subject to caution and yields an uncharacteristically high prefactor.

All the information about the initial and final coordinates of the species to diffuse (interstitial  $H_2$  and  $H_2O$ ) are available in the Supporting Information.

## Discussion

The analysis of the QENS data obtained for  $\beta$ - $Ca(BH_4)_2$  has shown that, within the time scale accessible by the two instruments used, two types of thermally activated hydrogen dynamics were observable in the temperature range from 90 to 320 K. The first type is described by localized H motion, that is, reorientations of the  $BH_4^-$  unit around the  $C_2$ -axis and  $C_3$ -axis. The experimental and DFT calculated energy barriers are in excellent agreement, giving  $E_{aC_2} = 0.14$  (0.15) eV and  $E_{aC_3} = 0.10$  (0.11) eV, experimental (calculated) values. The rotation about the  $C_3$ -axis is found to be energetically more favorable than the one around the  $C_2$ -axis.

The second type of hydrogen dynamics could not be described by rotational diffusion. With a Chudley–Elliot type  $Q$ -dependent broadening (nonlocalized event) giving a characteristic jump length of  $\sim 2.5$  Å, in agreement with the shortest H–H distance between two  $BH_4^-$  groups, a likely event would thus be a hydrogen–vacancy jump between neighboring groups. Nevertheless, the DFT results for this process indicated a slightly shorter jump length 2.1 Å, with the  $BH_3$  complex becoming planar, a higher energy barrier 0.46 eV, versus  $\sim 0.12$  eV experimentally, and a high energy for the formation of the vacancy (2.09 eV). All other vacancy-mediated diffusion mechanisms were also discarded because of their high energies of formation, thus interstitial H,  $H_2$ , and  $H_2O$  diffusions were studied.  $H_2$  interstitial diffusion gave results (0.09 eV, 2.1 Å) with the best agreement to the experimental one ( $\sim 0.12$  eV,  $\sim 2.5$  Å). Nevertheless, this latter result was obtained from only two experimental points,

and the  $H_2O$  interstitial diffusion cannot be strictly discarded. A possible explanation of the origin of  $H_2$  and/or  $H_2O$  interstitials is that they are formed during the synthesis of the compound. The MS measurement did not show any trace of water nor of oxygen, and the small release of hydrogen below 565 K correlates with the formation of an oxide phase. Given the oxygen free environment, the oxide possibly results from a reaction of the hydride with trapped interstitial water, or even THF, forming interstitial hydrogen that subsequently desorbs.

In  $LiBH_4$ , motion of entire  $BH_4^-$  units has been identified as the main mass transport mechanism above the melting temperature,<sup>45,46</sup> whereas at low temperatures, a net transport of atomic hydrogen, probed by hydrogen/deuterium exchange, was also observed, although at a very low rate.<sup>47,48</sup> From the results presented in this study, no such hydrogen dynamics have been detected, and it will be too speculative to conclude here that the observed translational diffusion of hydrogen is part of the mechanism for the bulk decomposition of  $Ca(BH_4)_2$ . The correlation between the QENS and DFT calculations indicates that, most probably, it is the diffusion of interstitial  $H_2$  that was observed; but it is probably due to a side reaction with trapped synthesis residue, leading to the partial oxidation of the compound and hydrogen release.

The combined DFT–QENS approach has been shown to be very useful both in the interpretation of the data and to determine crucial quantities useful to develop new experiments including the characteristic times and the energies barriers.

**Acknowledgment.** This work is based on experiments performed at the Swiss spallation neutron source SINQ, Paul Scherrer Institute, Villigen, Switzerland and at FRMII, JCNS Garching, Germany. The authors would like to acknowledge the European Graduate School for Sustainable Energy Technology and the Nordic Center for Excellence on Hydrogen Storage Materials. The Danish Center for Scientific Computing is acknowledged for super-computer access. The Center for Atomic Materials Design (CAMD) is supported by the Lundbeck Foundation. Financial support by EU-IP NESSHY (Contract #518271) and the ERA-NET project Hy-CO is also gratefully acknowledged.

**Supporting Information Available:** Initial and final coordinates of the species (interstitials  $H_2$  and  $H_2O$ ) to diffuse together with plots of the surrounding atoms. This material is available free of charge via the Internet at <http://pubs.acs.org>.

## References and Notes

- Züttel, A.; Rentsch, S.; Fischer, P.; Wenger, P.; Sudan, P.; Mauron, P.; Emmenegger, C. *J. Alloy. Compd.* **2003**, 356–357, 515.
- Nakamori, Y.; Miwa, K.; Ninomiya, A.; Li, H.; Ohba, N.; Towata, S.-I.; Züttel, A.; Orimo, S.-I. *Phys. Rev. B* **2006**, 74, 045126–1.
- Miwa, K.; Aoki, M.; Noritake, T.; Ohba, N.; Nakamori, Y.; Towata, S.-I.; Züttel, A.; Orimo, S.-I. *Phys. Rev. B* **2006**, 74, 155122–1.
- Severa, G.; Rönnebro, E.; Jensen, C. M. *Chem. Commun.* **2010**, 46, 421.
- Rönnebro, E.; Majzoub, E. H. *J. Phys. Chem. B* **2007**, 111, 12045.
- Kim, J.-H.; Shim, J.-H.; Cho, Y. W. *J. Power Sources* **2008**, 181, 140.
- Barkhordarian, G.; Jensen, T. R.; Doppiu, S.; Rösenberg, U.; Borgschulte, A.; Gremaud, R.; Cerenius, Y.; Dornheim, M.; Klassen, T.; Bormann, R. *J. Phys. Chem. C* **2008**, 112, 2743.
- Bée, M. *Quasielastic Neutron Scattering*; Adam Hilger: Philadelphia, PA, 1988.
- Richter, D.; Hempelmann, R.; Vinhas, L. A. *J. Less Common Met.* **1982**, 88 (2), 353.
- Campbell, S. I.; Kemali, M.; Ross, D. K.; Bull, D. J.; Fernandez, J. F.; Johnson, M. R. *J. Alloys Compd.* **1999**, 293–295, 351.
- Skiprov, A. V.; Udovic, T. J.; Rush, J. J. *Phys. Rev. B* **2007**, 76, 104305–1.



- (12) Skripov, A. V.; Udovic, T. J.; Cook, J. C.; Hempelmann, R.; Rempel, A. A.; Gusev, A. I. *J. Phys.: Condens. Matter* **2009**, *21*, 175410–5.
- (13) Voss, J.; Shi, Q.; Jacobsen, H. S.; Lefmann, K.; Zamponi, M.; Vegge, T. *J. Phys. Chem. B* **2007**, *111*, 3886.
- (14) Remhof, A.; Łodziana, Z.; Butcher, F.; Martelli, P.; Pendollino, F.; Friedrichs, O.; Züttel, A.; Embs, J. P. *J. Phys. Chem.* **2009**, *113*, 16834.
- (15) Verdal, N.; Hartman, M. R.; Jenkins, T.; DeVries, D. J.; Rush, J. J.; Udovic, T. J. *J. Phys. Chem. C* **2010**, *114*, 10027.
- (16) Butcher, F.; Łodziana, Z.; Remhof, A.; Friederichs, O.; Borgschulte, A.; Mauron, P.; Züttel, A.; Sheptyakov, D.; Barkhordarian, G.; Bormann, R.; Chlopek, K.; Fichtner, M.; Sørby, M.; Riktor, M.; Hauback, B.; Orimo, S. *J. phys. Chem. B* **2008**, *112*, 8042.
- (17) Filinchuk, Y.; Rönnebro, E.; Chandra, D. *Acta Mater.* **2009**, *57*, 732.
- (18) Łodziana, Z.; Vegge, T. *Phys. Rev. Lett.* **2004**, *93* (14), 145501.
- (19) Łodziana, Z.; Vegge, T. *Phys. Rev. Lett.* **2006**, *97* (11), 119602.
- (20) Filinchuk, Y.; Chernyshov, D.; Cerný, R. *J. Phys. Chem. C* **2008**, *112*, 10579.
- (21) Riktor, M. D.; Sørby, M. H.; Chlopek, K.; Fichtner, M.; Buchter, F.; Züttel, A.; C., H. B. *J. Mater. Chem.* **2007**, *17*, 4939.
- (22) Hunter, B. *IUCR Powder Diffraction Newsletter*, **1998**, 20.
- (23) Wuttke, J. To be published; [http://www.jcns.info/jcns\\_spheres](http://www.jcns.info/jcns_spheres).
- (24) <http://sinq.web.psi.ch/sinq/instr/mars.html>.
- (25) Wuttke, J. <http://www.messen-und-deuten.de/slwa>.
- (26) Azuah, R. T.; Kneller, L. R.; Qiu, Y.; Tregenna-Piggott, P. L. W.; Brown, C. M.; Copley, J. R. D.; Dimeo, R. M. *J. Res. Natl. Inst. Stan. Technol.* **2009**, *114*, 341.
- (27) Bahn, S. R.; Jacobsen, K. W. *Comput. Sci. Eng.* **2002**, *4*, 56.
- (28) Hammer, B.; Hansen, L. B.; Nørskov, J. K. *Phys. Rev. B* **1999**, *59*, 7413.
- (29) Kohn, W.; Sham, L. J. *Phys. Rev.* **1965**, *140*, 1133.
- (30) Vanderbilt, D. *Phys. Rev. B* **1990**, *41*, 7892.
- (31) Perdew, J. P.; Chevary, J. A.; Vosko, S. H.; Jackson, K. A.; Pederson, M. R.; Singh, D. J.; Fiolhais, C. *Phys. Rev. B* **1992**, *46*, 6671.
- (32) Liu, D. C.; Nocedal, J. *Math. Program.* **1989**, *45*, 503.
- (33) Henkelman, G.; Uberuaga, B. P.; Jonsson, H. *J. Chem. Phys.* **2000**, *113*, 9901.
- (34) Bitzek, E.; Koskinen, P.; Gähler, F.; Moseler, M.; Gumbusch, P. *Phys. Rev. Lett.* **2006**, *97*, 170201.
- (35) Vineyard, G. H. *J. Phys. Chem. Solids* **1957**, *3*, 121.
- (36) Mao, J.; Guoa, Z.; Poha, C. K.; Ranjbara, A.; Guoc, Z.; Yuc, X.; Liua, H. *J. All. Compd.* **2010**, *500*, 200.
- (37) Kim, Y.; Reed, D.; Lee, Y.-S.; Lee, J. Y.; Shim, J.-H.; Book, D.; Cho, Y. W. *J. Phys. Chem. C* **2009**, *113*, 5865.
- (38) Riktor, M. D.; Sørby, M. H.; Chlopek, K.; Fichtner, M.; B.C., H. *J. Mater. Chem.* **2009**, *19*, 2754–2759.
- (39) Riktor, M. D. To be published.
- (40) Levingston, R. C.; Rowe, J. M.; Rush, J. J. *J. Chem. Phys.* **1974**, *60*, 4541.
- (41) Wolf, D. *Solid State Commun.* **1977**, *23*, 853.
- (42) Didisheim, J. J.; Yvon, K.; Shaltiel, D.; Fischer, P. *Solid State Commun.* **1979**, *31*, 47.
- (43) Dickens, M. H.; Hayes, W.; Schnabel, P.; T., Hutchings M.; Lechner, R. E.; Renker, B. *J. Phys. C: Solid State Phys.* **1983**, *16*, L1.
- (44) Bender, O.; Schroeder, K. *Phys. Rev. B* **1979**, *19*, 3399.
- (45) Schoenflies, A. *Math. Ann.* **1889**, *34*, 172.
- (46) Shane, D. T.; Bowman, R. C.; Conradi, M. S. *J. Phys. Chem. C* **2009**, *113*, 5039.
- (47) Corey, R. L.; Shane, D. T.; Bowman, R. C.; Conradi, M. S. *J. Phys. Chem. C* **2008**, *112*, 18706.
- (48) Borgschulte, A.; Züttel, A.; Hug, P.; Racu, A. M.; Schoenes, J. *J. Phys. Chem. A* **2008**, *112*, 4749.
- (49) Gremaud, R.; Łodziana, Z.; Hug, P.; Willenberg, B.; Racu, A.-M.; Schoenes, J.; Ramirez-Cuesta, A. J.; Clark, S. J.; Refson, K.; Züttel, A.; Borgschulte, A. *Phys. Rev. B* **2009**, *80*, 100301–1.

JP107281V